Submitted to Physical Review C

LBL-7162
Preprint

FRAGMENTATION OF RELATIVISTIC ^{56}FE

G. D. Westfall, L. W. Wilson, P. J. Lindstrom, H. J. Crawford,
D. E. Greiner, and H. H. Heckman

October 1978

Prepared for the U. S. Department of Energy
under Contract W-7405-ENG-48

DISCLAIMER

LBL-7162

FRAGMENTATION OF RELATIVISTIC ^{56}FE

G.D. Westfall, Lance W. Wilson, P.J. Lindstrom, H.J. Crawford,
D.E. Greiner, and H.H. Heckman

Lawrence Berkeley Laboratory and Space Sciences Laboratory
University of California, Berkeley, California 94720

October 1978

ABSTRACT

The fragmentation of ^{56}Fe at 1.88 GeV/nucleon has been studied on H, Li, Be, C, S, Cu, Ag, Ta, Pb, and U targets. The detection apparatus consisted of a simple transmission detector. A method is presented which eliminates the effects of multiple interactions in the targets which were typically half an interaction-length thick. Elemental production cross sections, $\sigma(Z)$, were measured for Z = 13 to 25. Measured charge-changing cross sections, $\sigma_{\Delta Z \geq 1}$, and derived mass-changing cross sections, $\sigma_{\Delta A \geq 1}$, are presented for each target. The $\sigma(Z)$ factor into a term which depends only on the target and a term which depends only on the fragment observed. The $\sigma_{\Delta Z \geq 1}$ and $\sigma_{\Delta A \geq 1}$ follow a simple geometric behavior. The cross section for the removal of one proton from the ^{56}Fe projectile is enhanced for the heavier targets. This effect is described by a model assuming Coulomb dissociation. The $\sigma(Z)$ for ^{56}Fe on the H target are compared to the semiempirical formulae of Silberberg and Tsao.

KEY WORDS

NUCLEAR REACTIONS $H(^{56}Fe,X)$, $Li(^{56}Fe,X)$, $Be(^{56}Fe,X)$, $C(^{56}Fe,X)$, $S(^{56}Fe,X)$, $Cu(^{56}Fe,X)$, $Ag(^{56}Fe,X)$, $Ta(^{56}Fe,X)$, $Pb(^{56}Fe,X)$, $U(^{56}Fe,X)$, X = Al to Mn, measured elemental production cross sections; measured charge-changing cross sections and derived mass changing cross sections. Iron fragmentation cross sections, relativistic heavy ions, thick target corrections, coulomb dissociation.

I. INTRODUCTION

The fragmentation of light nuclei ($A \leq 16$) at relativistic energies (1-2 GeV/nucleon) has been studied extensively and several qualitative features have been established.[1-6] The fragments produced maintain most of their initial longitudinal velocity and the interactions have been described as dominantly peripheral. The momentum distributions of the fragments in the projectile rest frame are typically Gaussian, depend on the fragment, and are relatively independent of target mass and incident energy. The fragment production cross sections are also energy independent and can be factored into beam-fragment and target terms. These measurements have provided the basis for theoretical studies of the interaction process of high-energy nuclear collisions.[7-10] These cross sections have also been applied to quantitative calculations of cosmic ray propagation; for example, see Garcia-Munoz et al.[11]

With the recent acceleration of iron to relativistic energies at the Bevalac, the direct measurement of the astrophysically interesting fragmentation of iron is now possible. Presented here are the first iron fragmentation results using iron beams accelerated to relativistic energies. Using a simple transmission detector system, production cross sections for elements from $Z = 13$ to $Z = 25$ were measured for a variety of targets ranging from H to U. In addition, the charge-changing ($\sigma_{\Delta Z \geq 1}$) and mass-changing ($\sigma_{\Delta A \geq 1}$) cross sections were extracted. The mass-changing cross sections can be applied directly to calculations of cosmic ray propagation. The elemental production cross sections can be used to improve the semiempirical parameterizations of isotope production cross sections that enter into cosmic ray calculations.

Presented in Section II is a description of the experimental

apparatus. In Section III the data reduction technique is discussed. Results and systematics are presented in Section IV. Section V contains comparisons with other data and with the semiempirical formulae of Silberberg and Tsao.[12]

II. EXPERIMENTAL TECHNIQUE

A. Apparatus

The experimental setup is shown schematically in Fig. 1. The apparatus consisted of a beam definition module and an effective charge identification module. Each module was composed of lithium-drifted silicon detectors. The detectors were 3 mm thick and had 1500 mm^2 active area (44 mm diameter). The beam definition module contained two detectors and the effective charge module contained four detectors.

The targets used were typically half a mean free path in thickness. Cross sections for a hydrogen target were obtained by a subtraction of C from CH_2 targets. The targets used and their thicknesses are given in Table I.

A beam of approximately 10^3 particles/sec was focused on the apparatus. The beam spot was limited on the beam definition module by an active collimator. The collimator consisted of a plastic scintillator with a 1 cm diameter hole centered on the beam definition module. The scintillator operated as an anticoincidence tag. The lower threshold of the scintillator discriminator was set just below the signal from the beam. This setting prevented backscattered particles from producing an anticoincidence for otherwise good events.

Emulsion studies[13] of the fragmentation of Fe have shown that at

1.88 GeV/nucleon the projectile-like fragments with $Z \geqslant 3$ are limited to a narrow cone in the forward direction with an opening angle of about 3°. The effective charge module subtended a maximum angle from the beam axis ranging from 7° for beam particles interacting near the front edge of the target to 20° for interactions near the back edge of the target. Thus, the experiment was capable of measuring both the fragmentation cross section for the incident beam and the production cross sections for the high-Z fragments of the beam.

Since many of the interactions studied here produced several charged products, the effective charge module had several particles passing through it simultaneously. Particles with energies of 1-2 GeV/nucleon are minimum ionizing, so that the response of each silicon counter to a given particle was proportional to its charge squared. Therefore the effective charge module measures an effective charge, Z*, given by

$$Z^* = (\sum_i Z_i^2)^{1/2} \qquad (1)$$

where Z_i is the charge of a given particle and the sum is over all charged particles passing through the module.

If one of the particles passing through the module has a charge much larger than the remaining particles, its charge dominates the sum of squares. This effect is termed the leading charge effect and allows the association of Z* with the dominant charge.

B. Electronics

Each silicon detector was connected to a dual-gain charge-sensitive

preamplifier. The data presented in this paper were taken in the low gain mode. The analog signals were sent to separate linear amplifiers and analog-to-digital converters which relayed the digitized pulse height information to a PDP 11/45 computer through a CAMAC interface. The data were stored event-by-event on magnetic tape and the final analysis was done off-line on a CDC 7600 computer.

A good event was defined by a fast coincidence ($\approx$20 nsec) between the two detectors in the beam definition module. In addition, standard pileup rejection and dead time circuitry were employed to ensure the selection of single events. The only events analyzed were those where an acceptable beam particle was defined. Thus an absolute measure of the dead time was not necessary.

III. DATA REDUCTION

This section describes the major steps involved in the extraction of the cross sections given in Sec. IV. Because several of the techniques are new, the presentation is lengthy and detailed. Those more interested in the final results may want to proceed to Sec. IV.

A. Charge Identification

The calibration of the charge response of each counter (two beam defining and four fragment measuring) was accomplished by using the ΔE signals from uninteracted iron projectiles passing through the counters. The charge response was substantially higher when a target was in place than when no target was used. This effect is attributed to delta ray production in the target adding to the ΔE signal observed. The effect

was largest for the lighter targets and was of the order of a 5% increase in pulse height. The response of each counter to uninteracted iron projectiles was normalized to the projectile charge for each target.

Charge definition in both the beam defining and fragment measuring modules was accomplished by a multiple ΔE measurement. An average effective charge, $\bar{Z}$, was defined by

$$\bar{Z} = \frac{\sum_{i=1}^{D} \frac{Z_i}{\sigma_i^2}}{\sum_{i=1}^{D} \frac{1}{\sigma_i^2}} \qquad (2)$$

where Z_i and σ_i are the measured charge and charge resolution of the i^{th} counter, respectively, and D is the number of counters used. In addition, the consistency of the charge identification, χ^2, was expressed as

$$\chi^2 = \sum_{i=1}^{D} \frac{\left(Z_i - \bar{Z}\right)^2}{\sigma_i^2} \qquad (3)$$

Beam particle definition was accomplished with two detectors by requiring both that the average charge be within 0.45 charge units of the projectile and that χ^2 be less than 20. This definition eliminated $\approx$5% of the events. The charge resolutions of the two beam defining counters were 0.12 and 0.17 charge units respectively. A comparison of target-out to target-in results showed that backward scattered particles from the target did not affect the beam definition.

B. Zero Detector Thickness Extrapolation

In order to account for reaction losses in the four fragment measuring counters, a charge identification and consistency check was done separately for the first two counters as a unit, the first three counters as a unit, and all four counters as a unit. Thus for each event satisfying the beam particle definition requirements, an average charge and a χ^2 was assigned for 2, 3, and 4 consecutive detector identifications. A typical charge spectrum for four consecutive detector identifications using a carbon target is shown in Fig. 2. The peaks corresponding to leading charges down to 13 are clearly separable. These peaks were integrated to produce the number of events within a certain effective charge range that had a good χ^2 after passing through 2, 3 or 4 consecutive detectors. The results were then corrected for target-out background.

The χ^2 cuts were chosen to eliminate background. Since the number of degrees of freedom varies with the number of consecutive detectors used, the χ^2 cuts were chosen to eliminate a constant percentage of the data. The χ^2 cuts used were 6.63, 9.21, and 11.34 for 2, 3, and 4 consecutive detectors, respectively. These values correspond to the 99% value of a χ^2 distribution for 1, 2, and 3 degrees of freedom .

The requirement that an event with a given effective charge meet the χ^2 criteria for 2, 3, and 4 consecutive detectors led to an observable attenuation in the number of particles versus the number of consecutive detectors. In order to obtain the actual number of particles within a given effective charge range that exited the target (and

entered the detector stack), it was necessary to extrapolate to zero-detector thickness. Two slightly different algorithms were used for this extrapolation but both used the assumption that the attenuation was given by the expression

$$\eta_i = \eta_o \, e^{-\sigma_* D_i} \tag{4}$$

where η_i is the number of particles that have traversed D_i ($\equiv i + 1$) consecutive detectors, η_o is the number that originally entered the detector stack, and σ_* is the attenuation constant per detector. Note also that if the decrease in the number of particles is an irreversible loss process, the attenuation should have the property that the decreases have a Poisson distribution. Hence in the first algorithm it was assumed that the independent experimental differences $(\eta_i - \eta_{i+1})$ have the expectation value and variance of $\eta_i(1 - e^{-\sigma_*})$. A minimization of the statistic

$$\chi^2(\sigma_*) = \frac{(\eta_2 - \eta_1 e^{-\sigma_*})^2}{\eta_1 (1-e^{-\sigma_*})} + \frac{(\eta_3 - \eta_2 e^{-\sigma_*})^2}{\eta_2 (1-e^{-\sigma_*})} \tag{5}$$

yielded σ_* and its associated error. This best fit value for σ_* was then used to determine η_o and $\langle \delta\eta_o^2 \rangle$ via the equations

$$\eta_o = \frac{1}{3} \sum_i \eta_i \, e^{\sigma_* D_i}$$

$$\langle \delta\eta_o^2 \rangle^{1/2} = \frac{1}{3} \langle \delta\sigma_*^2 \rangle^{1/2} \sum_i \eta_i D_i \, e^{\sigma_* D_i} , \tag{6}$$

The second algorithm was less stringent and was used if any of the differences $(\eta_i - \eta_{i+1})$ were negative. In this algorithm it was assumed that the three experimental points were independent measurements with standard statistical errors. Thus, the parameters σ_* and η_o and their associated errors were determined from the simultaneous minimization of the statistic

$$\chi^2(\sigma_*, \eta_o) = \sum_{i=1}^{3} \frac{\left(\eta_i - \eta_o e^{-\sigma_* D_i}\right)^2}{\delta\eta_i^2} , \tag{7}$$

with $\delta\eta_i^2 \equiv \eta_i$.

The values for σ_* ranged from ≈ 0.07 for $\overline{Z} = 26$ to ≈ 0.15 for $\overline{Z} = 13$. The extrapolated values were approximately 15 - 35% greater than the number of good events in two consecutive detectors.

The two final steps in the extrapolation were the incorporation of counting statistics into the error on η_o and the extraction of the calibration constant k. The calibration constant corrects for the elimination of good events and was obtained from the equation

$$k = N_{beam}/(\eta_o)_{ZD,TO} \tag{8}$$

where N_{beam} is the number of beam particles in a run with target-out (TO) (as determined by the beam-definition module) and $(\eta_o)_{ZD,TO}$ is the zero detector thickness extrapolated (ZD) number of beam particles for the same TO configuration. For this experiment, k had the value 1.05. With

this value for k, the final values for η_o and $\langle \delta\eta_o^2 \rangle^{\frac{1}{2}}$ are given by the equations

$$\eta_o = k\ (\eta_o)_{ZD} \tag{9a}$$

and

$$\langle \delta\eta_o^2 \rangle^{1/2} = k \left(\langle \delta\eta_o^2 \rangle_{ZD} + (\eta_o)_{ZD} \right)^{1/2} . \tag{9b}$$

Note that it is the second term of equation (9b) that incorporates counting statistics into the extrapolation procedure.

Recall that the χ^2 cuts for charge identification were chosen to eliminate, in principle, only 1% of the valid events. The empirically based calibration constant, k, has the value 1.05. We attribute the difference between k and 1.01 to non-Gaussian tails in the resolution function for effective charge.

C. Thick Target Correction

As noted earlier, the target thicknesses were chosen such that approximately half of the particles entered the detector modules with a charge different from the beam's. That is, if p(n) ($\equiv \bar{n}^n e^{-\bar{n}}/n!$) is the probability for n charge-changing interactions while traversing such a target, then $p(o) \approx 1/2$, or equivalently, $\bar{n} \approx \ln 2$. This value for $\bar{n}$ means that approximately 15% of the fragments come from 2 or more interactions in the target. The correction for this thick target effect and the proper assignment of the errors introduced are discussed in the following section.

The formalism adopted for the removal of the effects of multiple interactions involves many of the concepts used in slab model calculations

for cosmic ray propagation.[14,15] However, in the cosmic ray calculations it is assumed that the cross sections are known and the total amount of target material is the unknown. In this experiment, the target material is measured while it is the cross sections that are unknown. This difference introduces some complexity into the analysis but doesn't change the formal description. Let $N_i(x)$ represent the number of particles of type i that have traversed x gm/cm^2 of target material, then, subject to the approximations given below, the equation for the change in $N_i(x)$ as a function of x is just

$$\frac{dN_i}{dx} = -\frac{\sigma_i}{m_T} N_i + \sum_j \frac{\sigma_{ij}}{m_T} N_j \quad , \qquad (10)$$

where σ_i is the mass-changing cross section for the i-th type, σ_{ij} is the total production cross section for the i-th type from the interactions of the j-th type, and m_T is the mass of the target material. Equation (10) is a continuity equation for the propagation through a uniform slab of material under the following assumptions:

1) The interactions that produce the fragments of interest are velocity preserving, i.e. the velocity shifts observed by Greiner et al.[2] are negligible.

2) The traversal time between target and detectors for unstable particles is much smaller than the mean decay time, which is true for all particle-stable nuclei.

3) There are no losses due to scattering outside of the solid angle subtended by the detectors.

4) The cross sections are independent of energy as observed by Lindstrom et al.[3] or, equivalently, that the cross sections are energy-averaged.

Equation (10) can be viewed as an ordinary differential equation for the column vector

$$\underline{N} = \begin{pmatrix} N_1 \\ \cdot \\ \cdot \\ \cdot \\ N_n \end{pmatrix}$$

especially if one introduces the matrix M whose entries are defined by the equation

$$M_{ij} = \begin{cases} -\sigma_i/m_T, & \text{if } i = j, \\ \sigma_{ij}/m_T, & \text{if } i \neq j \text{ and } j \text{ produces } i, \\ 0, & \text{otherwise} \end{cases} \tag{11}$$

With these definitions, equation (10) becomes

$$\frac{d\underline{N}}{dx} = M\underline{N} \, . \tag{12}$$

Under assumption (4), M is independent of x, so that the solution to equation (12) has the form

$$\underline{N} = \exp(Mx)\, \underline{N}_o \tag{13}$$

where N_o is the initial column vector and the matrix exp (Mx) is defined via the standard exponential power series. Note that, by ordering the species by increasing mass number, equation (11) shows that M becomes upper triangular with loss terms on the diagonal and production terms above. This ordering also means that the column vector N_o has the entries

$$(N_o)_i = \begin{cases} 0, \text{ if } i \neq n \\ N_B, \text{ for } i = n, \end{cases} \tag{14}$$

where N_B is the number of beam particles and n is the number of rows and columns of M.

Equation (13) is central to both the extraction of the cross sections and the assignment of errors. Note that in this experiment the measured quantities are N_B, x, and the sum of all N_i's that have the same charge, i.e. the various n_o's of equation (9), while the unknown cross sections are contained in the argument of the exponential. Moreover, the matrix M contains more entries for two different reasons. First, it contains the cross sections for both the beam and its fragments. Secondly, it contains the cross sections for the production and destruction of isotopes, not elements. The procedure adopted to cope with the first problem was to treat as known all cross sections that do not directly involve the fragmentation of the primary beam, or, equivalently, to treat as unknown only the cross sections that would be measured with a thin target. The second problem was handled by collapsing the matrix of isotopes into a matrix of elements. Details of this procedure are given below.

The generation of the "known" cross sections was greatly aided by the existence of semiempirical formulae for interactions with hydrogen and the fact that the production cross sections for nuclear interactions with heavier targets are proportional to those of hydrogen.[3] However, for the higher Z targets and for single nucleon removal, the process of relativistic coulomb dissociation also contributes to the rate of fragmentation.[9] Thus, it was assumed that the known cross sections for a target T, σ_{ij}^{T}, had the form

$$\sigma_{ij} = \gamma_T' \, \sigma_{ij}^{H} + \sigma_{ij}^{Coul} \tag{15}$$

where γ_T' denotes the proportionality constant, σ_{ij}^{H} denotes the semi-empirical cross section for a hydrogen target,[12] and σ_{ij}^{Coul} denotes the contribution from coulomb dissociation. Input assumptions for γ_T' were iterated until the input and output values were identical. Note that γ_T' is defined to be γ_T/γ_H, where γ_T is the target factor and γ_H is the hydrogen target factor (target factors are defined in Sec. IV). The procedure used to obtain σ_{ij}^{Coul} involved both an estimate of the total photoabsorption cross section via the Weizsäcker-Williams method and a self-consistent determination of the mean branching ratio for proton emission. See Appendix A for details.

The generation of the "known" mass-changing cross sections were also aided by systematics. In this case, our experimental charge-changing cross sections were parameterized using the Bradt-Peters form[16]

$$\sigma = \pi r_o^2 (A_T^{1/3} + A_B^{1/3} - b)^2 \tag{16}$$

using an effective A of 0.089 for the hydrogen target. To build equation (16) into a mass-changing cross section requires the addition of the cross section for neutron loss by either fragmentation or coulomb dissociation. That is, the i-th mass-changing cross section was assumed to have the form

$$\sigma_i = \pi r_o^2 (A_T^{1/3} + A_i^{1/3} - b)^2 + \gamma_T' \sum_{\ell<i} \sigma_{\ell i}^{H} + \sigma_{i' i}^{Coul} , \tag{17}$$

where the second term is the contribution from fragmentation (ℓ denotes other isotopes having the same Z as i) and the third term is the coulomb contribution (i' denotes an isotope with one less neutron than i).

In principle, the collapse of the matrix to elements should be performed after the exponentiation of equation (13). In practice, an approximation was introduced so that a collapse could take place prior to the exponentiation. This earlier collapse significantly reduced computing costs but retained much of the effect of the thick target. The actual prescription for the collapse was to assume that within a given element the fractional abundance of one of its isotopes could be approximated by the expression

$$W_j = \frac{\sigma_{j,Fe56}}{\Sigma \sigma'_{j,Fe56}} \tag{18}$$

where the sum in the denominator of equation (18) runs only over the

isotopes of the given element and where $\sigma_{j,Fe56}$ denotes the evaluation of equation (15) for the direct production of the j-th isotope from ^{56}Fe. In this way the production cross section for the I-th element from the J-th element, or equivalently, the collapsed matrix M_{IJ}, becomes

$$M_{IJ} = \sum_i \sum_j M_{ij} W_j \qquad (19)$$

where the double sums range only over the isotopes belonging to I and J. Note that the terms that contribute to M_{IJ} are not all of the same sign. This partial cancellation is the algebraic equivalent of converting a mass-changing cross section into a charge-changing cross section. Note also that in order to separate the behavior of the primary beam from its fragments, separate "element" groups were created for the ^{56}Fe beam and the set of all lighter isotopes of iron (denoted $Fe_{\neq}$). In this way, equation (19) was used to create a 15x15 matrix for the 13 elements from Al to Mn, the $Fe_{\neq}$ group, and the primary beam. Lastly, note that the error made by collapsing before exponentiation was studied by comparing the production cross sections obtained from the two procedures. This study showed the cross sections differed by approximately one per cent. By expanding each procedure in powers of the target thickness, one can show the difference is small because the approximation properly treats the lowest order term of the tertiary contributions.

In accordance with the conventions established for M_{ij}, the last column of M_{IJ} contains the cross sections that directly involve the primary beam, i.e. $\{M_{In}\}$ contains the parameters that are varied to yield a solution to equation (13). Recall that the zero-detector extrapolation

procedure gave values for the total number of particles exiting the target with a given charge. Thus equation (13) represents 14 separate equations. The 14 free parameters $(f_1,\ldots,f_{n-1})$ were chosen to be dimensionless scale factors to the 13 elemental production cross sections that directly involve the beam plus a scale factor to the mass-changing cross section for the primary beam. More explicitly, let $M'_{IJ}(f_1,\ldots,f_{n-1})$ be the matrix defined by

$$M'_{IJ}(f_1,\ldots,f_{n-1}) = \begin{cases} M_{IJ} & , \text{ if } J \neq {}^{56}\text{Fe} \\ f_I M_{IJ} & , \text{ if } J \leftrightarrow {}^{56}\text{Fe},\ I \neq \text{Fe} \\ M_{IJ} & , \text{ if } J \leftrightarrow {}^{56}\text{Fe},\ I \leftrightarrow \text{Fe} \\ f_{J-1} M_{JJ}, & \text{if } J \leftrightarrow {}^{56}\text{Fe} \end{cases} \tag{20}$$

Then the 14 f's are uniquely determined by the transcendental equations

$$N_I = \left[\exp(M' x)\right]_{In} N_B \quad , \text{ if } I = 1,\ldots,n-2 \tag{21a}$$

$$N_{n-1} = \sum_{I=n-1}^{n} \left[\exp(M' x)\right]_{In} N_B, \text{ otherwise.} \tag{21b}$$

Beginning with equation (21b), which yields f_{n-1}, the equations were solved by a regula falsi method which took advantage of the fact that the I-th equation only involved f_I and the previously determined $f_{I+1},\ldots,f_{n-1}$ for heavier fragments. The $\sigma(Z)$ are then found by scaling the entries of the last column of M by the appropriate f_I. By scaling the last entry of the last column the $\sigma_{\Delta A \geq 1}$ are obtained while the

$\sigma_{\Delta Z \geq 1}$ are found by combining the $\sigma_{\Delta A \geq 1}$ with the next-to-last entry. Although not immediately obvious from this formulation, it can be shown that the $\sigma_{\Delta Z \geq 1}$ are sensitive only to the ratio of incoming to outgoing iron particles.

The self-consistency of the thick target correction was established in two stages. First, for each target the measured charge-changing cross section was used to calculate the mean number of interactions. Secondly, artificial cross sections were obtained by assuming all of the observed fragments were pure secondaries of the primary beam. The resulting differences from the actual results were then shown to be completely consistent with the fraction of fragments expected to arise from more than one interaction.

The associated errors on the cross secions were derived from the rather involved matrix manipulations discussed in Appendix B. The errors represent the full propagation of the effects of 30% errors in the input production cross sections for a hydrogen target,[12] 7% errors in the input charge-changing cross sections, and 30% errors in the input Coulomb dissociation cross sections, as well as the errors from the extrapolation to zero detector thickness. Note that the assigned error on the charge-changing cross sections was obtained from the observed deviations from the parameterization of equation (16). The assigned error on the Coulomb dissociation cross section was estimated from its sensitivity to various input assumptions (see Appendix A).

IV. RESULTS AND SYSTEMATICS

A. Elemental Production Cross Sections

The elemental production cross sections, $\sigma(Z)$, for elements with $Z = 13$ to 25 produced from a relativistic ^{56}Fe beam are given in Table II and Fig. 3 for 10 different targets. The H target cross sections were obtained by subtracting the cross section for a C target from those for a CH_2 target. These cross sections are averaged over the energy loss in the thick targets. This energy loss was typically 0.15 GeV/nucleon, but ranged up to 1.00 GeV/nucleon for the Ta target. The energy loss of the 1.88 GeV/nucleon ^{56}Fe beam for each target is given in Table I. Corrections were made to the cross sections for target-out background, zero detector thickness extrapolation, and multiple interactions in the thick targets (see Sec. III). The stated errors include contributions from all of the above effects.

The distribution of elemental production cross sections for each target is generally nearly flat. No odd-even Z effects are visible. Exceptions to the general trend of flatness occur in the form of enhancement in the range $Z = 13$-17 and near $Z = 25$ for the heavier targets. The turnup at $Z = 25$ represents the Coulomb-enhanced removal of one proton from the projectile. This process depends on the charge of the target nucleus. The enhancement in the $Z = 13$-17 region can be attributed to the weakening of the leading charge effect. For heavy targets, this breakdown could be due to the production of multiple heavy fragments as seen for Fe interactions in emulsion.[13]

In previous work[3] with C and O projectiles, it was found that for fragments with more than one nucleon removed, the production cross

sections, σ_{BT}^{F}, could be factored into a term σ_T which depended only on the target, and a term σ_B^F which depended on the fragment and the beam. This empirical factorization was expressed as

$$\sigma_{BT}^{F} = \gamma_B^F \gamma_T. \tag{22}$$

Since the $\sigma(Z)$ for $Z = 25$ and the range $Z = 13$-17 are enhanced in the case of heavy targets, these cross sections were excluded from those used to determine the γ_T and γ_B^F. Hence, the γ_B^F and γ_T factors were obtained by minimizing the equation

$$\chi^2 = \sum_{T,F} (\sigma_{BT}^{F} - \gamma_T \gamma_B^F)^2 / \delta\sigma_{BT}^{F\,2}, \tag{23}$$

where T ranged over all targets but F was restricted to the range $Z_F = 18$-24. Note that the form of equation (22) allows for an arbitrary normalization of one of the factors. In accordance with convention,[3,17] this freedom is removed by assuming that γ_T for the carbon target is 1.92. The resulting target factors and their associated errors are given in Table III and Fig. 4.

The target factors can be fit by both a power law in the target mass number A_T and by a linear relationship to $(A_T^{1/3} + A_B^{1/3} - b)$. More explicitly, if the target factor has the form

$$\gamma_T = a\, A_T^{d}, \tag{24}$$

then the best fit values are a = 1.272 ± 0.044 and d = 0.177 ± 0.010 with a χ^2 of 9.9 for 8 degrees of freedom. The straight line in Fig. 4 corresponds to this fit. Similarly, if the target factor has the form

$$\gamma_T = c\ (A_T^{1/3} + A_B^{1/3} - b), \tag{25}$$

then the best fit values are c = 0.390 ± 0.024 and b = 1.2 ± 0.3 with a χ^2 of 5.8 for 8 degrees of freedom. The curved line in Fig. 4 corresponds to this second parameterization.

Recall that factorization failed to hold for the production of Mn (Z = 25) fragments (see Fig. 3). This failure results from the excitation and fragmentation of the projectile nucleus via its absorption of virtual photons from a target nucleus.[9] As discussed in Section II and Appendix A, a semiempirical model was used to compute the enhanced production of ^{55}Mn (and ^{55}Fe) via this process. This model assumed that the total photoabsorption cross section could be reliably estimated (to within 30%), but that the average branching ratio for proton emission had to be obtained from the data. Thus it was assumed that the Mn production cross section for a target T had the form

$$\sigma^T(\mathrm{Mn}) = \gamma^{\mathrm{Mn}}\ \gamma_T + r_p\ \sigma_T^{\mathrm{Coul}}, \tag{26}$$

where γ_T is the target factor from Table III, σ_T^{Coul} is the calculated photoabsorption cross section for producing ^{55}Mn, and where the two parameters are γ^{Mn} (the Mn fragment factor) and r_p (the mean branching ratio for protons). Values and error estimates for these parameters were obtained by minimizing the quantity

$$\chi^2 = \sum_T \frac{[\sigma^T_{obs}(Mn) - \sigma^T(Mn)]^2}{[(\delta\sigma^T_{obs}(Mn))^2 + \delta\sigma^T(Mn)^2]}, \quad (27)$$

where $\sigma^T_{obs}(Mn)$ is the observed cross section, $\delta\sigma^T_{obs}(Mn)$ is its associated error, and $\delta\sigma^T(Mn)$ is given by the expression

$$\delta\sigma^T(Mn)^2 = (\gamma^{Mn})^2 \delta\gamma_T^2 + r_p^2 (\delta\sigma_T^{Coul})^2 . \quad (28)$$

Note that $\delta\sigma_T^{Coul}$ was taken to be a constant 30% of σ_T^{Coul}. Also, note that equation (28) appears in the denominator of equation (27) because variations in equation (26) are comparable to the experimental uncertainties.

The eleven independent targets of Table I were used in the minimization of equation (27). The resulting best fit values were $r_p = 0.28 \pm 0.06$ and $\gamma^{Mn} = 85.0 \pm 4.9$ with a χ^2 of 13 for nine degrees of freedom. The value for r_p is consistent with an estimate of Weinstock and Halpern[18] and with experimental values for nearby nuclei.[19] The comparison of model and experiment is shown in Fig. 5. Note particularly that for the heaviest targets the enhancement represents a doubling of the cross section expected from the fragmentation systematics.

B. Charge-Changing and Mass-Changing Cross Sections

The charge-changing cross section, $\sigma_{\Delta Z \geq 1}$, is defined to be the cross section for the removal of at least one charge from the projectile. The measured charge-changing cross sections for a relativistic ^{56}Fe beam on 10 different targets are given in Table IV and Fig. 6. The charge-

changing cross sections contain the same energy averaging and experimental corrections as the elemental production cross sections. The errors given contain contributions from these effects.

Another quantity related to $\sigma_{\Delta Z \geq 1}$ is the mass-changing cross section, $\sigma_{\Delta A \geq 1}$, which is defined as the cross section for removing at least one nucleon. This cross section can be found from $\sigma_{\Delta Z \geq 1}$ by adding in the contribution from neutron loss that could not be measured in this experiment (see Sec. III). These values are also presented in Table IV and Fig. 6. The stated errors include errors in the added neutron loss contribution as well as those from the charge-changing cross sections.

The Bradt-Peters form of equation (16) was used to fit both the measured charge-changing and the derived mass-changing cross sections. For $\sigma_{\Delta Z \geq 1}$ and for all targets other than hydrogen, the best fit parameters were $r_o = 1.35 \pm 0.02$ fm and $b = 0.83 \pm 0.12$ with a χ^2 of 20 for 7 degrees of freedom. Similarly, for $\sigma_{\Delta A \geq 1}$, the best fit parameters were $r_o = 1.47 \pm 0.04$ fm and $b = 1.12 \pm 0.16$ with a χ^2 of 16. These fits are shown in Fig. 6.

V. COMPARISONS

The measured elemental production cross sections for the fragmentation of 1.88 GeV/nucleon ^{56}Fe on a H target can be compared to the semi-empirical model of Silberberg and Tsao.[12] This phenomenological model has been fit to a large range of high energy proton-nucleus results. As shown in Fig. 7, one finds the ratio of measured to calculated cross sections is generally greater than unity. The weighted

average of these ratios is 1.12 with a standard deviation of 0.27 for Z = 18 to 25. Thus, the semiempirical model is statistically consistent with the present experiment. Silberberg and Tsao have also made a preliminary attempt to parameterize production cross sections from nucleus-nucleus collisions.[20] However, as can be seen most clearly by comparing their form for the enhancement of one-nucleon removal with that seen in this experiment, further improvement is needed to achieve reasonable agreement with experiment.

A comparison can also be made with specific proton-nucleus experiments. Regnier[21] has used the technique of mass spectrometry to study the reaction of 1.05 and 24 GeV protons incident on a natural Fe target. Cumulative cross sections were measured for ^{38}Ar and ^{39}Ar and production cross sections for ^{36}Ar and ^{42}Ar were measured. Another proton-induced experiment was performed using mass spectrometry plus γ-ray spectrometry on an ultrapure natural Fe target at 0.6 and 21 GeV by Perron.[22] Using the semiempirical model of Silberberg and Tsao[12] to obtain the relative yields of isotopes within a given element, measurements equivalent to that of Regnier and Perron were generated. These comparisons are given in Tables VI and VII. Note that only if a cumulative cross section was both independent of the yield of the lighter isotopes of Fe and independent of significant contributions from the proton's interactions with other isotopes in the target was it used. In general, the present results fall between the lower and higher energy measurements of Regnier and Perron.

Measured charge-changing and mass-changing cross sections for a hydrogen target can be compared to the results of Renberg et al.[23]

for proton-nucleus total inelastic cross sections. The proton induced inelastic cross section on an Fe target was measured at 230-550 MeV and at 2800 MeV. These cross sections show little energy dependence. Therefore, one can compare the present results at 1.88 GeV/nucleon. The $\sigma_{\Delta Z \geq 1}$ and $\sigma_{\Delta A \geq 1}$ are both within errors of agreeing with the average proton total inelastic cross section of 696 ± 7 mb. This agreement indicates that the total inelastic cross section is nearly equal to the fragmentation cross section for a H target. However, no such claim is being made for other targets.

VI. CONCLUSIONS

Many of the systematics observed in the previous C and O projectile work are confirmed in the present Fe fragmentation. The elemental production cross sections factor into a target term and a beam-fragment term. These target factors can be parameterized by a power law in the target mass number, A_T, or a linear relationship in $A_T^{1/3} + A_B^{1/3}$, where A_B is the beam mass number. The derived power law exponent of 0.177 ± 0.010 is lower than the 0.25 value found to be consistent with the C and O target factors. The measured charge-changing and extracted mass-changing cross sections follow a geometric behavior similar to the previous results.

Whereas the hydrogen target factor follows the systematics of the other targets, the charge-changing and mass-changing cross sections for the hydrogen target do not. In Fig. 6 one can see that the hydrogen target cross sections fall significantly below the straight line. In order to bring the hydrogen target results into agreement with the

systematics, an effective A_T of 0.089 rather than 1.0 can be used.

The observed enhancement of one proton removal from the ^{56}Fe projectile for the heaviest targets is explained in terms of the projectile being excited by the absorption of a virtual photon from the target nucleus as was observed in the C and O fragmentation. Within the assumptions of the model used to predict the enhancement, the mean branching ratio for proton emission was determined to be 0.28 ± 0.06.

The present experiment is consistent with previous proton-nucleus results. The measured elemental production cross sections for the hydrogen target are higher than the predictions of the semiempirical model of Silberberg and Tsao by a factor of 1.12, but are still in statistical agreement.

ACKNOWLEDGEMENTS

We wish to thank H.A. Grunder, R.J. Force, and the Bevatron operations staff for their considerable efforts in providing the iron beam. We especially thank F.S. Bieser and C.P. McParland for their dedicated contributions to electronics design and on-line computing. We also thank E.E. Beleal, D.M. Jones, and R.C. Zink for their contribution to the equipment fabrication and data handling. This work was carried out under the auspices of the Nuclear Physics Division of the U.S. Department of Energy, Contract W-7405-ENG-48 and the National Aeronautics and Space Administration, Grant NGR-05-003-513.

APPENDIX A

This appendix describes the means adopted to estimate the cross sections for the Coulomb dissociation of both the primary beam and its fragments.

Essentially, the procedure is to follow the approach of Heckman and Lindstrom,[9] who showed that by using the Weizsäcker-Williams method of virtual quanta, the cross section can be written in the form

$$\sigma_{WW} = \int_{\omega_o} \sigma_\nu(\omega) N(\omega) d\omega \qquad (A1)$$

where $\sigma_\nu(\omega)$ is the photonuclear cross section at photon energy ω ($\hbar = c = 1$), $N(\omega)$ is the number of virtual photons per unit energy, and ω_o is the threshold for the photo process. Following the treatment of Jackson[24]

$$N(\omega) = (2q^2/\pi\omega\beta^2)\left\{ xK_o(x)K_1(x) - (\beta^2x^2/2)\left(K_1^2(x) - K_0^2(x)\right)\right\} \qquad (A2)$$

where $x = \omega b_{min}/\gamma\beta$, b_{min} is the minimum impact parameter, q is the charge on the particle "providing" the virtual photons, and the K's are modified Bessel functions. Heckman and Lindstrom wrote b_{min} in terms of the 10% charge density radius points of the beam and target ($r_{0.1}^{B,T}$). They showed that if the form

$$b_{min} = r_{0.1}^{B} + r_{0.1}^{T} - d \qquad (A3)$$

were used with experimental data for $\sigma_\nu(\omega)$ and equation (A2) for $N(\omega)$, then d had a value consistent with 0. Therefore, for this work, equation (A3) was used for b_{min} with the further assumption that d was negligibly small.

Heckman and Lindstrom were able to use published photonuclear data for ^{12}C and ^{16}O. In general, some phenomenological estimate is required. This estimate is aided by the fact that σ_ν is dominated by absorption at the giant dipole resonance. For intermediate and heavy nuclei a droplet model for the giant dipole resonance[25] has been successful in reproducing the A dependence and energies of the resonance. This model predicts that the resonance frequency, ω_{GDR}, is given by the expression (eq. (4.12) of ref. 25 with $m \to m^*$)

$$(\omega_{GDR})^{-2} = \frac{m^* R_o^2}{8J}\left(1 + u - \frac{1+\varepsilon+3u}{1+\varepsilon+u}\,\varepsilon\right) \tag{A4}$$

where $\varepsilon = 0.0768$, $u = (3J/Q)A^{-1/3}$, $Q = 17$ MeV, $J = 36.8$ MeV, $R_o = r_o A^{1/3}$, $r_o = 1.18$ fm, $m^* = 0.7\ m_u$, and m_u = mass of nucleon. The model has less success in quantitatively predicting the widths of the resonances so that "reasonable" values of (5 ± 2) MeV had to be used.[26]

Taking maximum advantage of the relevant sum rules and assuming that the resonance has a Lorentz shape[26] leads to the form

$$\sigma_\nu(\omega) = \frac{\sigma_m}{1 + [(\omega^2 - \omega_{GDR}^2)^2/\omega^2\Gamma^2]}, \tag{A5}$$

with $\sigma_m = \sigma_{TRK}/(\pi\Gamma/2)$. The Thomas-Reiche-Kuhn cross section, σ_{TRK},[27] is given by the equation

$$\sigma_{TRK} = 60(NZ/A) \text{ MeV mb} \quad . \tag{A6}$$

The resonant frequency is given by equation (A4) and $\Gamma = (5 \pm 2)$ MeV.

Equations (A1), (A2), and (A5) yield the total photoabsorption cross section, i.e. a cross section independent of the modes of de-excitation. Also, after taking into account both the variations of the calculation as a function of the width Γ and the simplicity of the model, each total absorption cross section was assigned an error of 30%. In order to use the equations for proton and neutron emission (assumed to be the only important modes), one needs a way of estimating the branching ratios. For the incident beam, this estimate was done in a self-consistent way using the enhanced production of Mn for heavy targets. That is, the assumed branching ratio for the (γ,p) reaction was varied until consistent with the observed enhancement (see Sec. IV). For the secondary beams, an ad hoc form was chosen that reproduced the slope (near Fe) of the proton branching ratio curve of Weinstock and Halpern[18] and that gave the value found for the primary beam. In addition, it was assumed that the ratio (which is normally suppressed by the Coulomb effect) would not exceed the fraction of protons in the nucleus. The expression that incorporates all of these features is

$$r_p = \min \left| Z/A,\ ae^{-bZ} \right| \tag{A7}$$

with $a = 1.95$ and $b = 0.075$.

One technical point remains. Equation (A2) depends on kinetic energy while the cross sections were assumed to be energy independent. Moreover, because the variable x of equation (A2) depends on $\gamma\beta$ and because of the significant energy losses given in Table I, there can be a 20% variation in the density of virtual photons between the front and back of the target. To minimize this effect, an average production location was used. For the targets involved in this experiment, the average location of a primary's interaction was approximately half the full target thickness, while the average location of a secondary's interaction was approximately two-thirds. Thus, for the primary beam, energy loss tables were used to compute the kinetic energy/nucleon at the half-thickness. The resulting values of β and γ were used in equations (A1) and (A2) and yielded the total cross sections given in Table A1. For the secondary beams, the "recipe" was slightly more involved because part of the energy loss takes place while a primary. In this case the kinetic energy at the two-thirds thickness point was computed by combining the energy loss of the primary at the half-thickness point with the additional energy loss of the secondary while traversing the remaining one-sixth distance. The resulting values of β and γ were then used in equation (A2).

APPENDIX B

This appendix describes the detailed manipulations involved in obtaining proper error assignments for the cross sections.

Recall that the cross sections arise from the (n-1) transcendental equations given in equation (21) of the text. In order to achieve a

greater conciseness of presentation, it is convenient to introduce the $(n-1) \times n$ matrix D defined by the relation

$$D_{ij} = \begin{cases} 1, \text{ if } i = j \\ 1, \text{ if } i = n-1 \text{ and } j=n \\ 0, \text{ otherwise} \end{cases} . \tag{B1}$$

Using this definition, equation (21) can also be written as

$$N_I = \left[D \exp (M'x) \right]_{In} N_B . \tag{B2}$$

Also, variations in the f's can be obtained from the equation

$$\delta N_I = \left[D \, \delta \exp (M'x) \right]_{In} N_B . \tag{B3}$$

In the scalar case $\delta(\exp m\, x) = x\delta m \exp (m\, x)$, and the analog to equation (B3) is easily manipulated. However, for matrices this is not possible because $\delta M'$ and M' do not commute.[28] If the perturbation is small enough to expand in powers of $\delta M'$ then as shown in ref. 28,

$$\delta\left(e^{M'x}\right) \approx \int_0^x e^{M'(x-x')} \, \delta M' e^{M'x'} \, dx' . \tag{B4}$$

Next, reexpress $\delta M'$ as the sum of three matrices. That is, let

$$\Delta_1 = \left(\overbrace{\begin{matrix} \\ 0 \end{matrix}}^{n-1} \left| \begin{matrix} (f_1-1)\ \delta M_{1n} \\ \vdots \\ (f_{n-2}-1)\,\delta M_{n-2,n} \\ 0 \\ (f_{n-1})\,\delta M_{nn} \end{matrix} \right. \right\} n \qquad \text{(B5)}$$

and

$$\Delta_2 = \left(\overbrace{\begin{matrix} \\ 0 \end{matrix}}^{n-1} \left| \begin{matrix} \delta f_1\ M_{1n} \\ \vdots \\ \delta f_{n-2}\ M_{n-2,n} \\ 0 \\ \delta f_{n-1}\ M_{nn} \end{matrix} \right. \right\} n \qquad \text{(B6)}$$

so that

$$\delta M' = \delta M + \Delta_1 + \Delta_2 \qquad \text{(B7)}$$

where M is the matrix of the "known" cross sections and δM is the associated error matrix. Also, using the summation convention for indices other than n, define the (n-1) by (n-1) matrix $B_{II'}$, by the expression

$$B_{II'} = \begin{cases} D_{Ii} \int_0^x \left[e^{M'(x-x')}\right]_{iI'} M_{I'n} \left[e^{M'x'}\right]_{nn} N_B dx', & \text{if } I'=1,\ldots,n-2 \\ D_{Ii} \int_0^x \left[e^{M'(x-x')}\right]_{in} M_{nn} \left[e^{M'x'}\right]_{nn} N_B dx', & \text{if } I'=n-1 \end{cases} \tag{B8}$$

and a column vector of length (n-1) by the equation

$$C_I = D_{Ii} \int_0^x \left[e^{M'(x-x')}\right]_{ik} \left[\delta M + \Delta_1\right]_{k\ell} \left[e^{M'x'}\right]_{\ell n} N_B dx' \quad . \tag{B9}$$

Then substituting equation (B7) into (B4) and rearranging the terms via equations (B8) and (B9) one obtains the equation

$$(\delta f)_I = (B^{-1})_{II'} \left[\delta N_{I'} - C_{I'}\right], \tag{B10}$$

where the second term contains the effects of errors in the matrix of "known" cross sections. Returning to dimensional units means the variations in the I-th of the (n-1) deduced cross sections (in cm^2/g) are given by

$$\delta\sigma_I = \begin{cases} \delta f_I \, M_{In} + f_I \, \delta M_{In} & \text{if } I=1,\ldots,n-2 \\ \delta M_{n-1,n} + \delta f_{n-1} M_{nn} + f_{n-1} \, \delta M_{nn} & \text{if } I=n-1 \end{cases} \tag{B11}$$

Next, invoke the simplifying assumption of uncorrelated errors in δN and

δM. Then, by using equations (B10) and (B11), the diagonal terms of the error matrix with $I = 1,\ldots,n-2$ have the form

$$\begin{aligned}\langle \delta\sigma_I^2\rangle = &\left[(B^{-1})_{IK}M_{In}\right]^2 \langle \delta N_K^2\rangle + f_I^2 \langle \delta M_{In}^2\rangle \\ &+ (B^{-1})_{IK}(B^{-1})_{IK'}(M_{In})^2 \langle C_K C_{K'}\rangle \\ &- 2(B^{-1})_{IK}M_{In}f_I \langle C_K \delta M_{In}\rangle .\end{aligned} \tag{B12}$$

Similarly, the final term has the form

$$\begin{aligned}\langle \delta\sigma_{n-1}^2\rangle = &[B^{-1}{}_{n-1,n-1}M_{nn}]^2 \langle \delta N_{n-1}^2\rangle + f_{n-1}^2\langle \delta M_{nn}^2\rangle + \langle \delta M_{n-1,n}^2\rangle \\ &+ (B^{-1})_{n-1,n-1}(B^{-1})_{n-1,n-1}(M_{nn})^2 \langle C_{n-1}C_{n-1}\rangle \\ &- 2(B^{-1})_{n-1,n-1}M_{nn}f_{n-1} \langle C_{n-1}\delta M_{nn}\rangle \\ &- 2(B^{-1})_{n-1,n-1}M_{nn} \langle C_{n-1}\ \delta M_{n-1,n}\rangle\end{aligned} \tag{B13}$$

when full advantage is taken of the upper triangular nature of M and B.

Next, define a three-dimensional array C_{Ikl} (related to C_I) by the equation

$$C_{Ikl} = D_{Ii}\int_0^x \left[e^{M'(x-x')}\right]_{ik}\left[e^{M'x'}\right]_{ln} N_B dx' .$$

and a two-dimensional array G_{Kl} by the equation

$$G_{Kl} = D_{Ki} \int_0^x \left[e^{M'(x-x')} \right]_{il} \left[e^{M'x'} \right]_{nn} N_B dx' \quad .$$

Substituting these definitions into equation (B12) gives

$$\begin{aligned} \langle \delta\sigma_I^2 \rangle = & \left[M_{In} (B^{-1})_{IK} \right]^2 \langle \delta N_K^2 \rangle + f_I^2 \langle \delta M_{In}^2 \rangle \\ & + (M_{In})^2 (B^{-1})_{IK} C_{Klm} (B^{-1})_{IK} C_{K\,lm} \langle (\delta M + \Delta_1)_{lm}^2 \rangle \\ & - 2 f_I M_{In} (B^{-1})_{IK} G_{KI} \langle (\delta M + \Delta_1)_{In} \delta M_{In} \rangle \quad . \end{aligned} \tag{B14}$$

Substituting into equation (B13) gives

$$\begin{aligned} \langle \delta\sigma_{n-1}^2 \rangle = & \left[M_{nn} (B^{-1})_{n-1,n-1} \right]^2 \langle \delta N_{n-1}^2 \rangle + f_{n-1}^2 \langle \delta M_{nn}^2 \rangle \\ & + \langle \delta M_{n-1,n-1}^2 \rangle + \left[M_{nn} (B^{-1})_{n-1,n-1} C_{n-1,lm} \right]^2 \langle (\delta M + \Delta_1)_{lm}^2 \rangle \\ & - 2 f_{n-1}^2 M_{nn} (B^{-1})_{n-1,n-1} G_{n-1,n} \langle \delta M_{nn}^2 \rangle \\ & - 2 M_{nn} (B^{-1})_{n-1,n-1} G_{n-1,n-1} \langle \delta M_{n-1,n}^2 \rangle \quad . \end{aligned} \tag{B15}$$

The errors given in the text were obtained from equations (B14) and (B15). Note that these equations express the error in the σ's in terms of the errors in N (i.e. from counting and extrapolation) and in terms of the errors in the "known" cross sections (assumed to be 30%

for the off-diagonal terms and 7% for the diagonal terms).

Several technical points are in order. First, it was found that Simpson's rule for a nine-point grid was sufficient to calculate the integrals of the exponentiated matrices. Also, the necessary terms were calculated recursively from the first grid point. Lastly, in all cases requiring the determination of exp(Rx) for either a "large" R or x, use was made of the identity

$$\exp(Rx) = [\exp(Rx/n)]^n. \tag{B16}$$

That is, if Rx were too big to permit rapid convergence of the power series, then a value of n was found so that exp (Rx/n) did rapidly converge. Equation (B16) was then used to recover exp (Rx).

REFERENCES

1. H.H. Heckman, D.E. Greiner, P.J. Lindstrom, and F.S. Bieser, Phys. Rev. Lett. 28, 926 (1972).
2. D.E. Greiner, P.J. Lindstrom, H.H. Heckman, B. Cork, and F.S. Bieser, Phys. Rev. Lett. 35, 152 (1975).
3. P.J. Lindstrom, D.E. Greiner, H.H. Heckman, Bruce Cork, and F.S. Bieser, Lawrence Berkeley Laboratory Report No. LBL-3650, unpublished (1975).
4. L.M. Anderson, Lawrence Berkeley Laboratory Report No. LBL-6769, (Ph.D. thesis), unpublished (1977).
5. J. Papp, Lawrence Berkeley Laboratory Report No. LBL-3633 (Ph.D. thesis), unpublished (1975).
6. H.H. Heckman, D.E. Greiner, P.J. Lindstrom, and H. Shwe, Phys. Rev. C 17, 1735 (1978).
7. A.S. Goldhaber, Phys. Lett. 53B, 306 (1974).
8. N. Masuda and F. Uchiyama, Phys. Rev. C 15, 1598 (1977), and Phys. Rev. C 15, 972 (1977).
9. H.H. Heckman and P.J. Lindstrom, Phys. Rev. Lett. 37, 56 (1976).
10. J.V. Lepore and R.J. Riddell, Jr., Lawrence Berkeley Laboratory Report No. LBL-3086, unpublished (1974).
11. M. Garcia-Munoz, G.M. Mason, and J.A. Simpson, Ap. J. 201, L141 (1975).
12. R. Silberberg and C. H. Tsao, Astrophys. J. 25, suppl. 220, 315 (1973), and Proceedings of the 15th Int. Cosmic Ray Conference, Plovdiv 2, 84 (1977).
13. P.S. Freier and C.J. Waddington, Astrophys. and Spa. Sci. 38, 419 (1975), and E.M. Friedlander, private communication (1978).

14. Lance W. Wilson, Lawrence Berkeley Laboratory Report LBL-7723, (Ph.D thesis), unpublished (1978).

15. R. R. Daniels and S. A. Stephens, Space Science Rev. 17, No. 1, 45 (1975).

16. H. C. Bradt and B. Peters, Phys. Rev. 77, 54 (1950).

17. G. M. Raisbeck and F. Yiou, Phys. Rev. Lett. 35, 155 (1975).

18. E. V. Weinstock and J. Halpern, Phys. Rev. 94, 1651 (1954).

19. B. L. Berman, private communication (1978).

20. R. Silberberg and C. H. Tsao, Proceedings of the 15th Int. Cosmic Ray Conference, Plovdiv, 2, 89 (1977).

21. S. Regnier, Proceedings of the 15th Int. Cosmic Ray Conference, Plovdiv, 2, 76 (1977).

22. C. Perron, Phys. Rev. C 14, 1108 (1976).

23. P. U. Renberg, D. F. Measday, M. Pepin, P. Schwaller, B. Favier, and C. Richard-Serre, Nucl. Phys. A183, 81 (1972).

24. J. D. Jackson, Classical Electrodynamics (Wiley, New York), 2nd ed., 719 (1975).

25. W. D. Myers, W. J. Swiatecki, T. Kodama, L. J. El-Jaick, and E. R. Hilf, Phys. Rev. C 15, 2032 (1977).

26. B. L. Berman and S. C. Fultz, Rev. Mod. Phys. 47, 713 (1975).

27. J. S. Levinger, Photo-Nuclear Dissociation (Oxford University, London), (1960).

28. R. Bellman, Introduction to Matrix Analysis (McGraw-Hill, New York, 1970), 2nd ed., p. 174.

TABLE I. Target thickness and energy loss in each target.

Target	Thickness (g/cm^2)	Energy Loss (GeV/nucleon)
CH_2	4.65, 6.98	0.12, 0.18
Li	5.42	0.10
Be	7.15	0.14
C	6.63	0.14
S	12.1	0.24
Cu	33.9	0.60
Ag	43.8	0.72
Ta	68.5	1.00
Pb	43.2	0.60
U	48.5	0.65

Table II. Elemental production cross sections for 1.88 GeV/nucleon ^{56}Fe beams in mb.

TARGET Z	H	LI	BE	C	S	CU	AG	TA	PB	U
13	25+/-10	50+/- 5	50+/- 7	83+/-11	78+/-18	179+/-27	112+/-19	81+/-14	191+/-37	307+/-79
14	31+/- 9	57+/- 5	75+/- 8	57+/-10	106+/-14	72+/-11	158+/-20	115+/-20	119+/-22	169+/-28
15	22+/-10	57+/- 6	57+/- 8	59+/-10	50+/- 8	88+/-15	64+/-13	133+/-20	78+/-16	176+/-34
16	37+/-24	56+/- 6	63+/- 8	54+/-10	74+/-12	56+/-11	96+/-13	109+/-17	116+/-19	116+/-22
17	36+/-17	38+/- 4	54+/- 7	53+/- 7	66+/-14	86+/-13	79+/-14	101+/-18	90+/-19	133+/-22
18	31+/- 9	55+/- 6	54+/- 7	55+/- 9	74+/-13	95+/-15	84+/-14	100+/-18	73+/-15	113+/-19
19	36+/- 9	56+/- 5	65+/- 7	52+/- 7	55+/-21	88+/-14	79+/-11	111+/-20	90+/-19	105+/-15
20	47+/-11	64+/- 6	68+/- 7	78+/-11	97+/-14	98+/-14	118+/-14	107+/-17	144+/-22	143+/-19
21	62+/-11	67+/- 6	77+/- 8	54+/- 9	91+/-13	100+/-15	104+/-13	129+/-18	111+/-17	153+/-21
22	82+/-13	75+/- 6	83+/- 9	87+/-11	64+/-10	101+/-14	124+/-16	152+/-19	148+/-22	95+/-16
23	60+/-11	88+/- 7	88+/- 9	100+/-11	86+/-12	121+/-15	117+/-15	150+/-19	142+/-20	181+/-27
24	80+/-13	98+/- 7	111+/- 9	124+/-13	128+/-16	149+/-16	218+/-21	206+/-22	242+/-25	208+/-22
25	127+/-24	141+/-18	156+/-21	181+/-27	250+/-22	219+/-20	280+/-23	457+/-34	509+/-40	646+/-43

Table III. Target factors, γ_T, and fragment factors, γ_B^F, for a 1.88 GeV/nucleon ^{56}Fe beam.

Target	γ_T	Fragment	γ_B^F
H	1.40 ± 0.10	Ar	28.8 ± 1.3
Li	1.78 ± 0.04	K	29.8 ± 1.3
Be	1.93 ± 0.07	Ca	37.8 ± 1.4
C	1.92 ± 0.09	Sc	37.3 ± 1.4
S	2.03 ± 0.13	Ti	41.0 ± 1.5
Cu	2.63 ± 0.13	V	46.2 ± 1.5
Ag	2.94 ± 0.14	Cr	60.7 ± 1.6
Ta	3.36 ± 0.17		
Pb	3.31 ± 0.19		
U	3.40 ± 0.18		

Table IV. Charge-changing cross sections, $\sigma_{\Delta Z \geq 1}$, and mass-changing cross sections, $\sigma_{\Delta A \geq 1}$, for 1.88 GeV/nucleon ^{56}Fe.

Target	$\sigma_{\Delta Z \geq 1}$ (b)	$\sigma_{\Delta A \geq 1}$ (b)
H	0.68 ± 0.04	0.75 ± 0.05
Li	1.34 ± 0.03	1.43 ± 0.04
Be	1.57 ± 0.03	1.67 ± 0.05
C	1.56 ± 0.05	1.66 ± 0.06
S	2.07 ± 0.08	2.22 ± 0.09
Cu	2.71 ± 0.07	2.94 ± 0.10
Ag	3.34 ± 0.08	3.71 ± 0.14
Ta	4.34 ± 0.08	4.97 ± 0.20
Pb	4.33 ± 0.15	5.10 ± 0.27
U	5.02 ± 0.11	5.92 ± 0.29

Table V. Comparison of measured vs. calculated elemental production cross sections, $\sigma(Z)$, for 1.88 GeV/nucleon ^{56}Fe incident on a H target. The calculated cross sections were obtained using the semiempirical model of Ref. 12.

Z	$\sigma(Z)$ measured (mb)	$\sigma(Z)$ calculated (mb)	$\frac{\sigma(Z) \text{ measured}}{\sigma(Z) \text{ calculated}}$
13	25 ± 10	17	1.47 ± 0.59
14	31 ± 9	22	1.41 ± 0.41
15	22 ± 10	22	1.00 ± 0.45
16	37 ± 24	29	1.28 ± 0.83
17	36 ± 17	26	1.24 ± 0.59
18	31 ± 9	39	0.79 ± 0.23
19	36 ± 9	26	1.38 ± 0.35
20	47 ± 11	35	1.34 ± 0.31
21	62 ± 11	35	1.77 ± 0.31
22	82 ± 13	67	1.22 ± 0.19
23	60 ± 11	55	1.09 ± 0.20
24	80 ± 13	90	0.89 ± 0.14
25	127 ± 24	87	1.46 ± 0.28

Table VI. Comparison of the production cross sections for proton-induced fragmentation of Fe (Ref. 21) to those obtained in this experiment for Fe incident on a H target at 1.88 GeV/nucleon. The cross section for the production of a specific isotope was found using Ref. 12 to scale the appropriate $\sigma(Z)$.

Fragment	Cross Sections (mb) at 1.05 GeV	at 24 GeV	Equivalent Cross Section at 1.88 GeV	Fraction(s) of $\sigma(Z)$[b]
^{36}Ar	2.49 ± 0.32	1.37 ± 0.18	2.11 ± 0.61	0.068
^{38}Ar[a]	18.2 ± 1.9	9.8 ± 1.3	18.3 ± 4.5	0.0010(S), 0.044(Cl), 0.486(Ar), 0.042(K), 8.1×10^{-4}(Ca)
^{39}Ar[a]	9.02 ± 0.95	4.97 ± 0.65	5.7 ± 1.7	0.0097(Cl), 0.174(Ar)
^{42}Ar	0.112±0.016	0.084±0.012	0.071±0.021	0.0023

[a]Denotes an experimentally cumulative cross section which sums the yields of both the fragment and its short-lived parent isotopes.

[b]Ref. 12 has been used to obtain the isotope fractions. In cases of cumulative cross sections, fractions are given for each of the elements that contributes.

Table VII. Comparison of the production cross sections for proton-induced fragmentation of Fe (Ref. 22) to those obtained in this experiment for Fe incident on a H target at 1.88 GeV/nucleon. The cross section for the production of a specific isotope was found using Ref. 12 to scale the appropriate $\sigma(Z)$.

Fragment	Cross Sections (mb) at 0.6 GeV	at 21 GeV	Equivalent Cross Section at 1.88 GeV	Fraction(s) of $\sigma(Z)$[b]
^{45}Sc[a]	27.9 ± 1.9	18.0 ± 1.9	30.1 ± 4.2	5.1×10^{-4}(K), 0.023 (Ca), 0.369(Sc), 0.075(Ti)
^{46}Sc	8.45± 0.27	6.0 ± 0.5	7.9 ± 1.4	0.127
^{48}V[a]		12.1 ± 1.3	16.1 ± 2.8	0.251(V), 0.013(Cr)
^{49}V[a]	38.0 ± 3.0	18.6 ± 3.2	28.7 ± 4.6	0.419(V), 0.045(Cr)
^{50}V	18.0 ± 1.1	10.0 ± 1.6	10.0 ± 1.8	0.166
^{51}V	6.8 ± 1.0	2.9 ± 0.6	3.0 ± 0.5	0.0019(Ti), 0.047 (V)
^{50}Cr	27.2 ± 2.8	15.1 ± 2.4	18.1 ± 2.8	0.214(Cr), 0.0074 (Mn)
^{51}Cr[a]	43.8 ± 1.7	25.1 ± 3.2	31.8 ± 4.4	0.328(Cr), .044 (Mn)
^{53}Cr[d]	11.8 ± 1.8	8.5 ± 1.7	6.6 ± 1.1	0.0017(V), 0.081(Cr)
^{54}Mn	33.3 ± 1.6	29.2 ± 2.7	39.2 ± 7.4	0.309(Mn)

[a] Denotes an experimentally cumulative cross section which sums the yields of both the fragment and its short-lived parent isotopes.

[b] Ref. 12 has been used to obtain the isotope fractions. In cases of cumulative cross sections, fractions are given for each of the elements that contributes.

Table A1. The calculated total photoabsorption cross section for 1.88 GeV/nucleon ^{56}Fe incident on various targets.

Target	σ^{coul}(mb) [a]
H	---
Li	2
Be	3
C	7
S	46
Cu	130
Ag	306
Ta	629
Pb	834
U	1008

[a] Parameters were Γ = 5 MeV, ω_o = 10 MeV.

FIGURE CAPTIONS

Fig. 1 Schematic diagram of experimental apparatus.

Fig. 2 Effective charge spectrum for 1.88 GeV/nucleon incident on a C target.

Fig. 3 Measured elemental production cross sections for 1.88 GeV/nucleon ^{56}Fe incident on ten different target nuclei. The cross sections for each successive target are suppressed by a factor of 10.

Fig. 4 Extracted target factors for fragments with Z = 18-24 from 1.88 GeV/nucleon ^{56}Fe incident on ten targets. The straight line corresponds to a parameterization of the form $\gamma_T = aA_T^d$. The curved line represents a parameterization of the form $\gamma_T = c(A_T^{1/3} + A_B^{1/3} - b)$. See text for discussion of parameterizations.

Fig. 5 Comparison of the Mn production cross sections for 1.88 GeV/nucleon ^{56}Fe incident on ten targets to the results predicted using the fragmentation systematics. The theory shown is calculated assuming that the removal of one proton from the projectile is enhanced by the Coulomb field of the target.

Fig. 6 Mass-changing and charge-changing cross sections for 1.88 GeV/nucleon ^{56}Fe incident on 10 different targets. The straight lines correspond to parameterizations of the form $\sigma = \pi r_o^2(A_T^{1/3} + A_B^{1/3} - b)^2$ as discussed in the text.

Fig. 7 Ratio of the measured elemental production cross sections on a hydrogen target to those calculated using the semiempirical

model of Silberberg and Tsao.[12] The dashed line shows the weighted average of 1.12 for fragments with Z = 18-25.

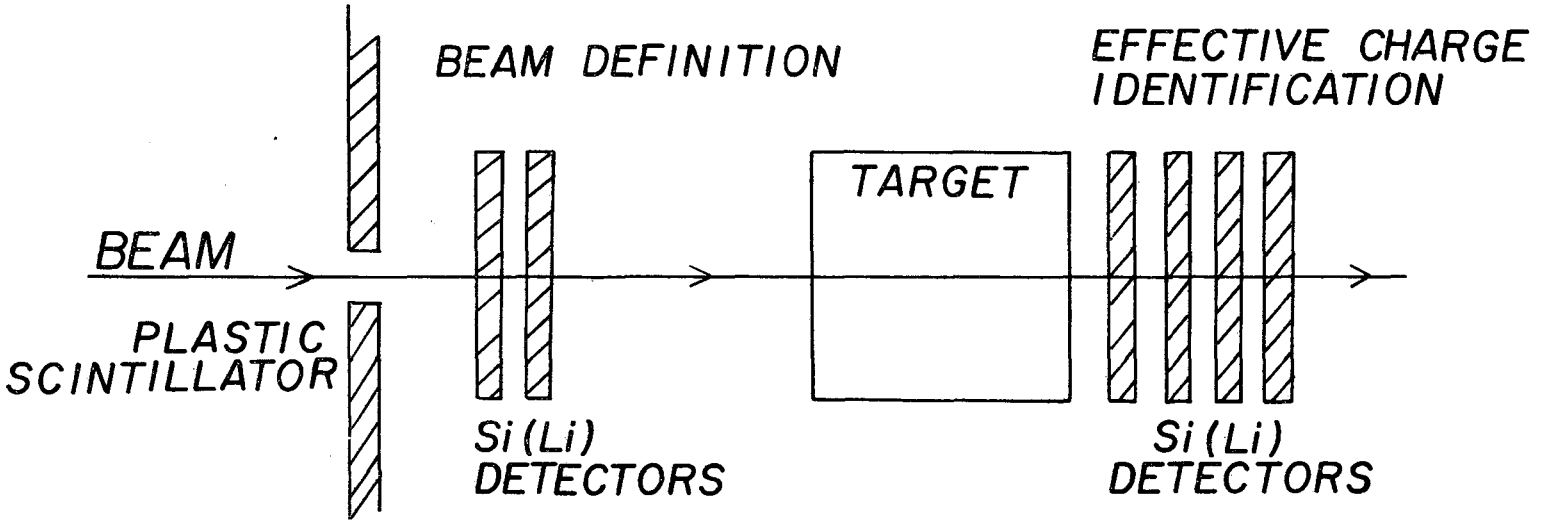

XBL 7810-11929

Fig. 1

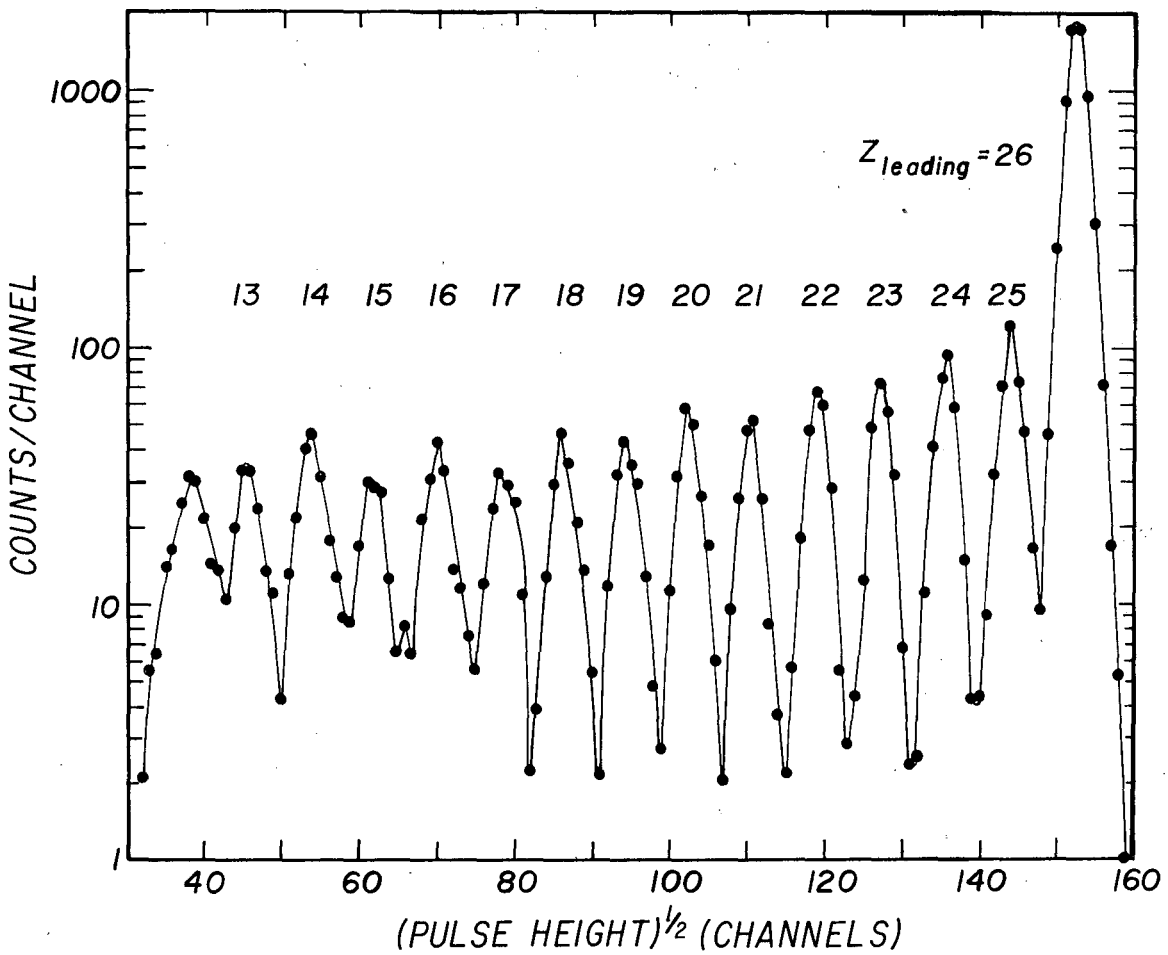

XBL 781-6748

Fig. 2

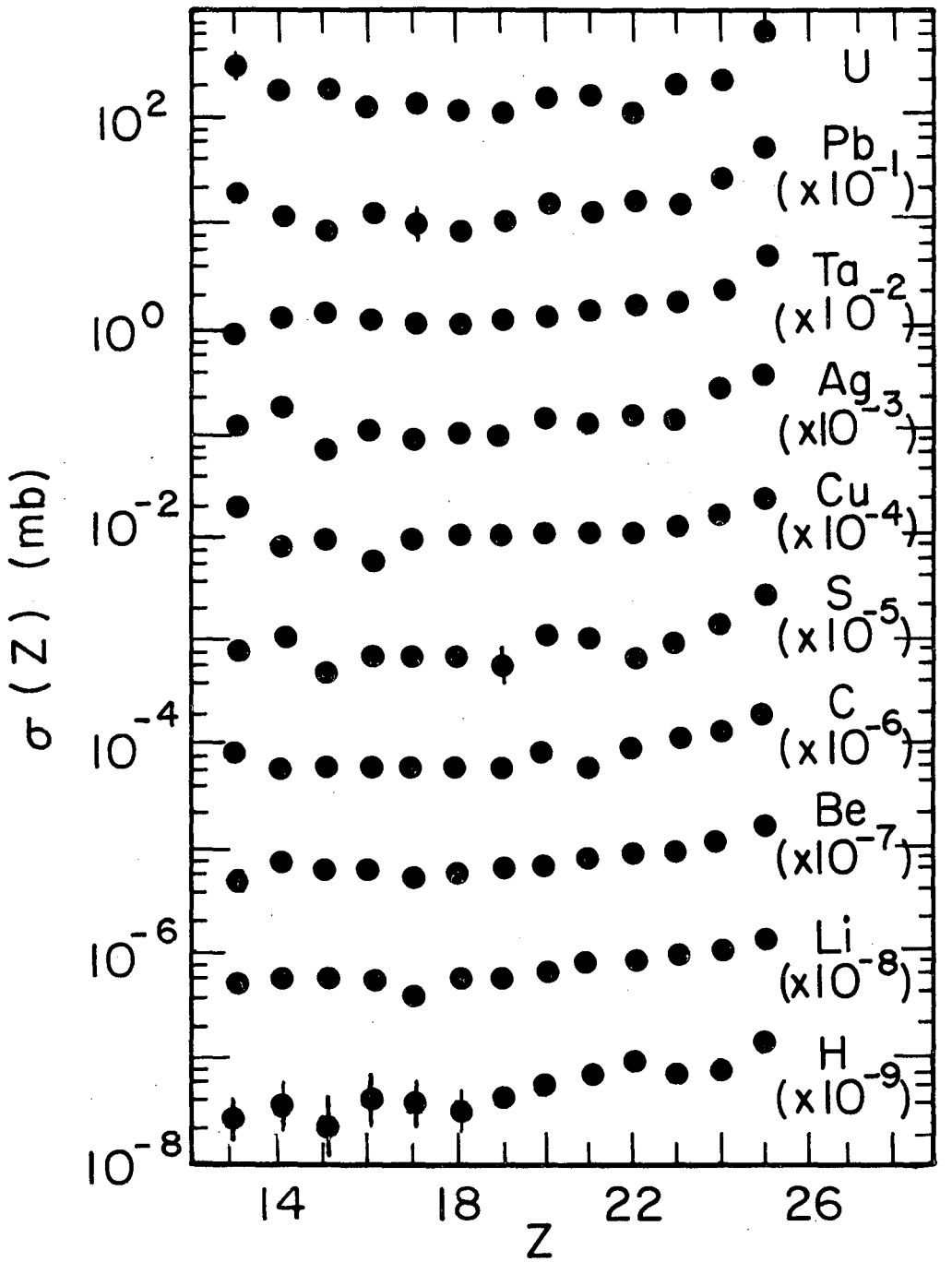

XBL7810-11519

Fig. 3

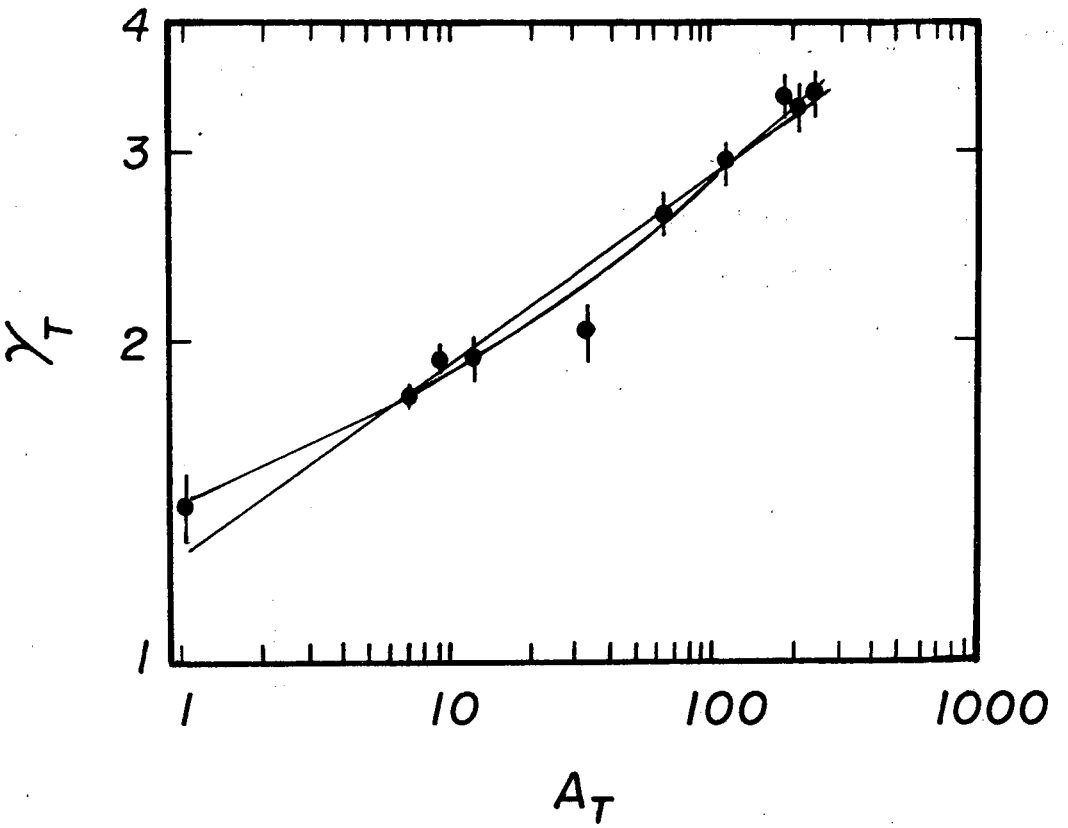

XBL 788-10139

Fig. 4

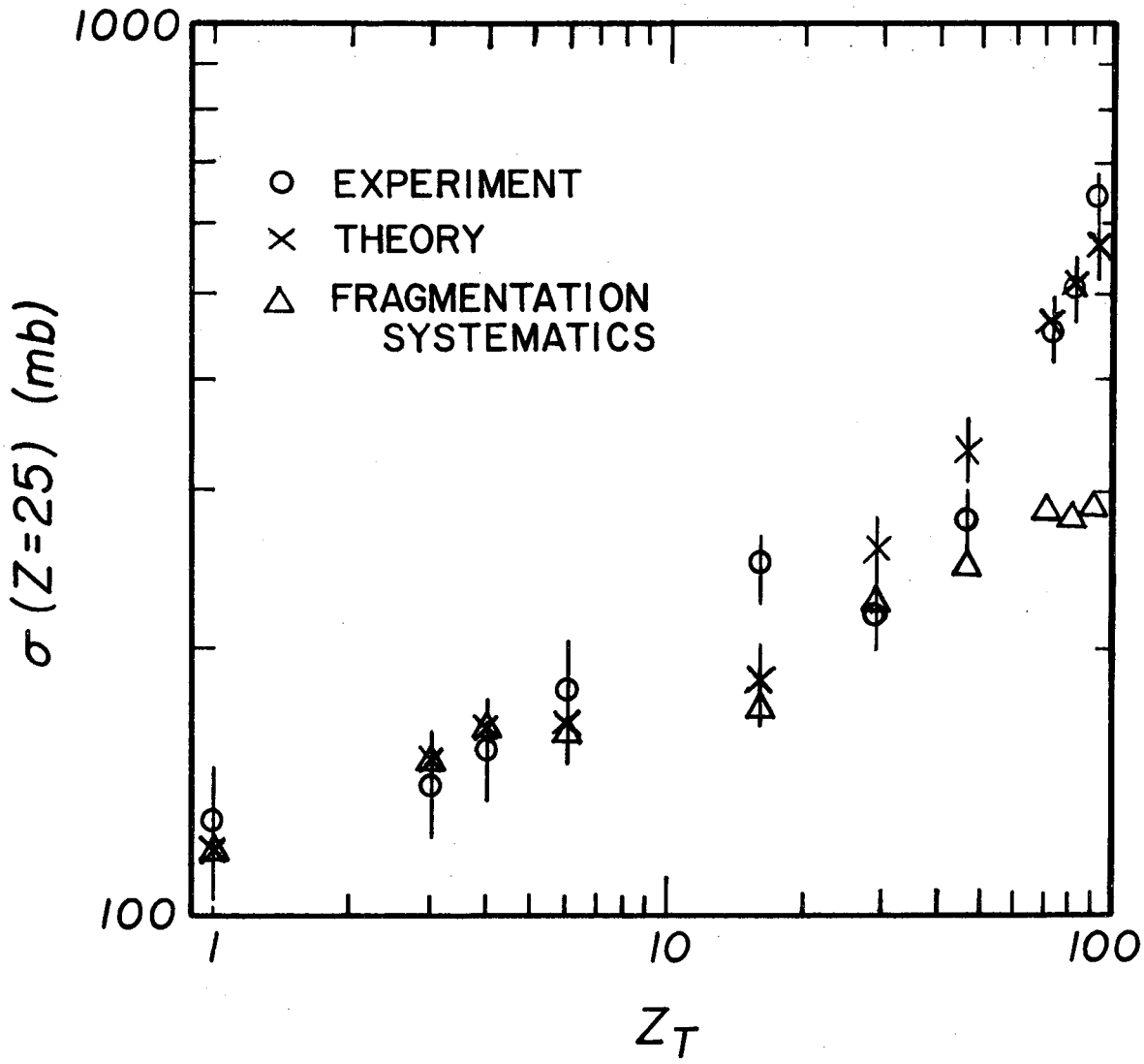

XBL 788-10140

Fig. 5

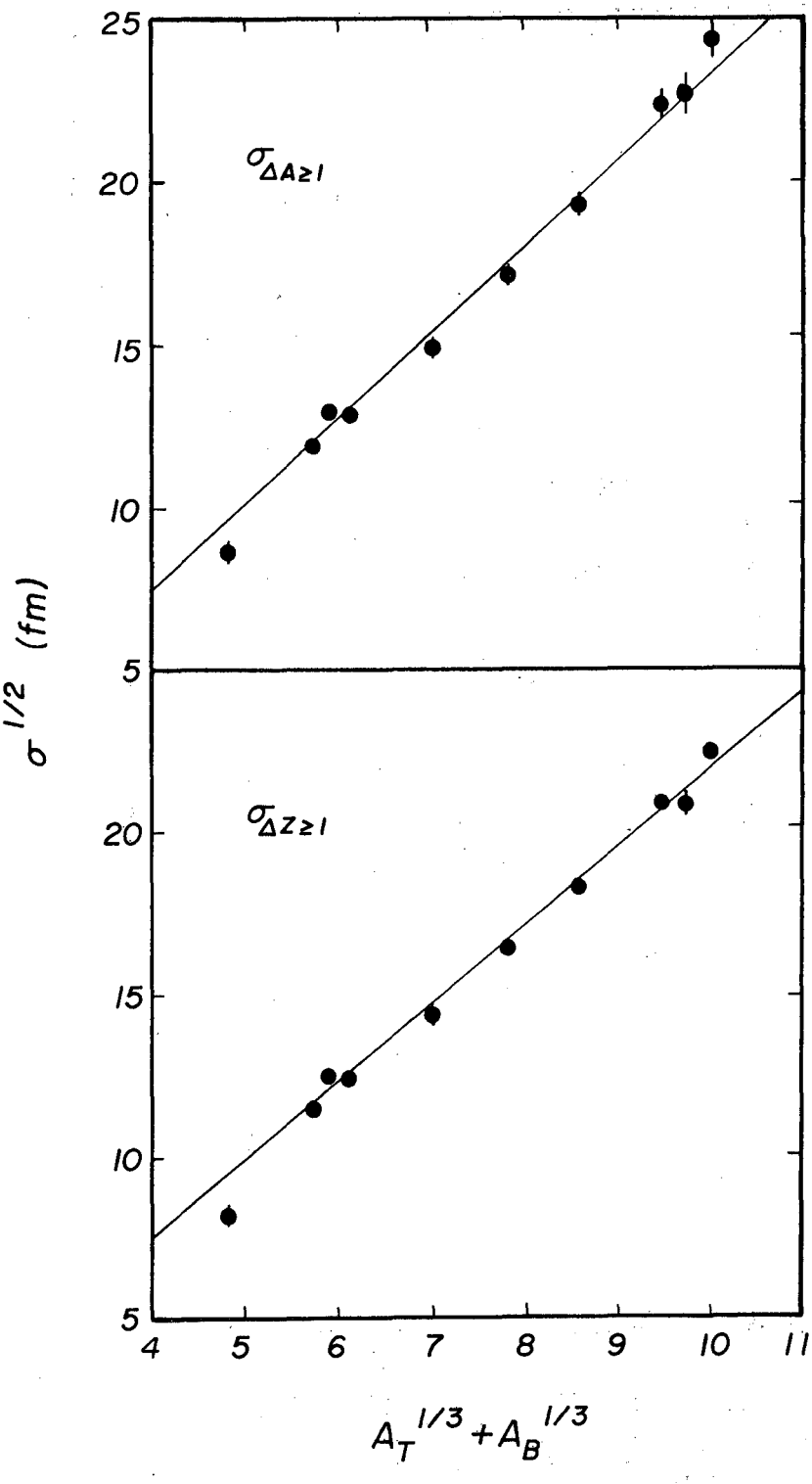

XBL 788-10138

Fig. 6

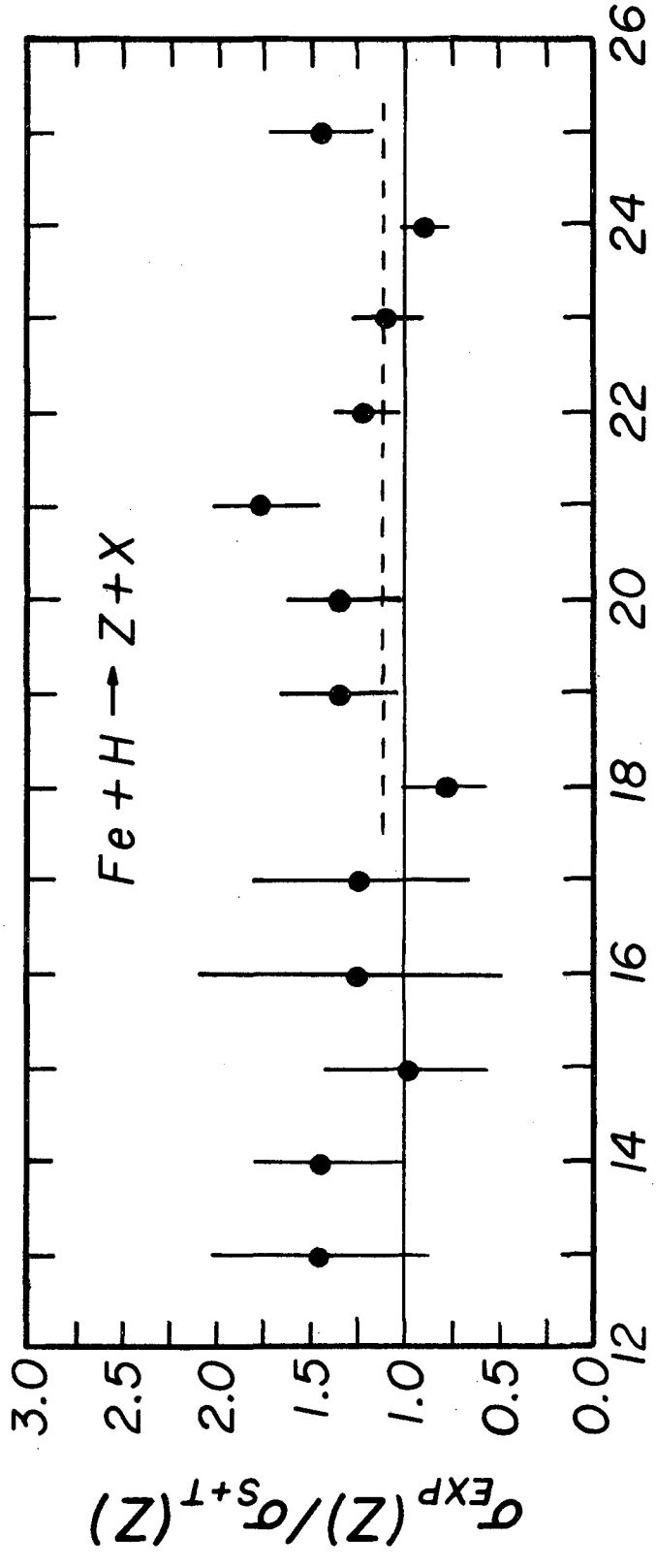

XBL 7810-11930

Fig. 7

TECHNICAL INFORMATION DEPARTMENT
LAWRENCE BERKELEY LABORATORY
UNIVERSITY OF CALIFORNIA
BERKELEY, CALIFORNIA 94720